

Evaluation of thinning behaviour under the influence of plastic hardening and surface friction during small punch test

S. C. Pandit, N. A. Alang*, I. U. Ferdous, J. Alias, M. F. Hassan, A. H. Ahmad

Faculty of Mechanical and Automotive Engineering Technology, Universiti Malaysia Pahang Al-Sultan Abdullah, 26600, Pekan Pahang, Malaysia

sarthokchandrapandit@gmail.com, azuan@umpssa.edu.my, imam.ul.ferdous@gmail.com, juliawati@umpssa.edu.my, firdaus@umpssa.edu.my, asnul@umpssa.edu.my



Citation: Pandit, S. C., Alang, N. A., Ferdous, I. U., Alias, J., Hassan, M. F., Ahmad, A. H., Evaluation of thinning behaviour under the influence of plastic hardening and surface friction during small punch test, *Fracture and Structural Integrity*, 72 (2025) 46-61.

Received: 25.10.2024

Accepted: 09.01.2025

Published: 11.01.2025

Issue: 04.2025

Copyright: © 2025 This is an open access article under the terms of the CC-BY 4.0, which permits unrestricted use, distribution, and reproduction in any medium, provided the original author and source are credited.

KEYWORDS. Deformation, Friction, Hardening, Small Punch, Thinning.

INTRODUCTION

Material used in nuclear reactors, power generation, or chemical processing plants are exposed to critical conditions like high temperatures, pressure, radiation, and corrosive environments. The high temperature components made from these materials suffer from various damage mechanisms such as aging, creep, corrosion, embrittlement, and swelling, which can greatly degrade their properties, especially during prolong exposure. This degradation leads to microstructural damage that may expand to a macroscopic level over the service time and eventually hamper the operation of the entire facility [1]. Proper regular inspection of these components is required to identify any unintended damage and monitor its progression. Mechanical testing, such as uniaxial tensile tests, compression tests and creep tests are common practices to determine the remaining lifespan of these materials. However, the abovementioned tests typically require robust equipment, which is expensive and complex especially when long-term duration is necessary, as in creep test [2] Furthermore, conventional test procedures require a larger material sample, usually obtained from the extraction of the real component in service. In this context, a relatively new technique called the small punch (SP) test can potentially address the aforementioned issues. The small punch test apparatus is relatively simple and inexpensive, requiring minimal resources for setup and operation. Moreover, the small punch test typically offers faster testing times, making it more suitable for rapid



material screening or quality control applications. Interestingly, the small punch test requires relatively small specimens and causes negligible damage after extraction from the components.

In the small punch test, the specimen is clamped between two circular upper and lower dies, and force is applied at the center of the specimen by means of the punch. As the punch moves vertically, the specimen is subjected to punch's load and deforms. This deformation process continues until a fracture occurs as the punch penetrates the specimen. The deformation process of the material under the small punch load can be divided into five distinct zones, namely: (a) linear elastic bending (Zone I), (b) plastic bending (Zone II), (c) membrane stretching (Zone III), (d) plastic instability (Zone IV), and (e) fracture (Zone V) [1]. Linear elastic bending (Zone I) is the zone where the deformation is directly proportional to the applied load. The stress and strain are within the elastic limit, and the material will return to its original shape once the load is removed. In plastic bending of Zone II, the material undergoes significant bending and plastic flow, resulting in permanent deformation. In membrane stretching of Zone III, the plastic deformation continues, and the material experiences bending under biaxial stress states. As the force is further applied, the material enters plastic instability in Zone IV. In this deformation zone, the material reaches a critical stress level, resulting in a local reduction of the material's thickness or necking. Fracture (Zone V) is the final zone that represents the complete failure of the material, typically resulting in separation of the specimen. Prior to fracture, cracks initiate and then progress under the load. From the load vs. displacement curve, several mechanical properties like yield strength, ultimate tensile strength, ductility, fracture toughness, creep properties and fatigue data and can be determined [1].

Although the small punch test is a relatively simple method and offers several advantages over conventional mechanical testing, its results can be influenced by various factors. Among them, friction is a main concern reported by researchers [3]. When a load is applied on the specimen through the punch, a friction force is induced at the contact surface between the punch and the specimen. Additionally, friction can also be induced between the die and the specimen. These frictions can significantly affect the result obtained from the small punch test. Alang et al. [4] reported that the fracture behaviour of the specimen and the strain distribution are influenced by friction. In another study, Campitelli et al. [5] claimed that the friction effect becomes apparent when displacement is greater than 0.5 mm. The maximum load that can be sustained by the material is higher under friction compared to the case where friction is negligible. Similarly, Yang et al. [6] found that the friction coefficient between the punch and specimen controls the initiation and crack propagation in the material. When the friction coefficient increases, the necking starts earlier, eventually leading to crack initiation. Cortellino et al. [7] applied Leu's friction model in numerical simulation and observed a significant change in the load-displacement curve. In contrast, Arunkumar et al. [8] reported that the load-displacement curve remains nearly similar under both dry and lubricated conditions. The deformation mechanism under the influence of friction is not well understood due to its complexity and is currently still in debate among researchers.

Another important factor that may influence the deformation response of the material is plastic hardening. The plastic hardening varies by the heat-to-heat variation as well as the manufacturing processes. Plastic deformation significantly increases the number of dislocations in the material structure. These dislocations eventually increase the strength of the deformed materials [9]. Yang et al. [10] studied the plastic hardening behaviour of a Fe-16Mn-10Al-0.86C-5Ni high-specific-strength steel during uniaxial tensile deformation. They found that when this steel is stretched, the force and stretch are distributed among the grains. Some grains stretch first, followed by others, until all of them stretch together. In another study, Choudhary et al. [11] investigated the plastic hardening behaviour of 9Cr-1Mo steel. They applied the Voce equation and Kocks-Mecking approach which demonstrated that plastic-hardening behaviour varies significantly with temperature and strain rate. Hence, understanding the deformation response of plastic hardened material is necessary. Tantideeravit et al. [12] conducted Finite Element (FE) simulations on the SP test of plastic-hardened SM490A carbon steel and claimed that the yield and ultimate strength are influenced by plastic hardening. This observation is further strengthened by Calaf-Chica et al [13], who conducted FEM analysis on plastic hardened materials and found that yield strength and ultimate tensile strength increases with hardening. Sánchez-Ávila et al. [14] performed SPT on hardened and annealed 316L stainless steel and demonstrated that hardening significantly affects localized thinning and strain rate evolution during punching. Similarly, Peng et al. [15] employed coupled plastic hardening with damage evolution models like Swift-Voce and demonstrated that how hardening influences deformation uniformity in SPT. In another study, Kuna et al. [16] investigated the effect of hardening parameters on different steel under small punch load and found that hardening parameters have significant effects on SPT results. They employed two axisymmetric FEM models during finite element analysis: a) a comprehensive model incorporating all apparatus components to account for elastic compliance b) a simplified model focusing solely on the elastoplastic deformation of the specimen, treating the punch and die as rigid bodies. The simplified model provided a better agreement with the experimental results compared to the comprehensive setup, with errors remaining below 10%. Moreover, the material was modeled as elastoplastic with isotropic hardening, to capture realistic mechanical behavior during loading. Study by Maier et al. [17] allows precise calibration of hardening parameter like isotropic



hardening modulus, facilitating a characterization of material's plastic hardening under small punch loading. Clearly, FEM can be a reliable method for analyzing and validating small punch tests.

Under small punch test, the load is applied locally at center point of the specimen. Upon load application, higher deformation occurs at the center while other regions experience less deformation depending on the stress distribution in the specimen. In fact, the upper surface of the sample tends to deform more than the bottom surface. As a result, the so called ‘thinning’ phenomenon, characterized by the reduction of thickness, is observed. Thinning can be measured as the displacement difference between the top and bottom points of the specimen in the through-thickness direction and can be expressed as in Eqn. (1)

$$T = \delta_{UN} - \delta_{LN} \tag{1}$$

where, δ_{UN} and δ_{LN} are the nodal displacement of top and bottom nodes, respectively.

Researchers continuously explore thinning behaviour observed in SPT using advanced measurement systems. Egan et al. [18] used optical measurement to precisely track the height and width changes of specimen. This approach allows direct observation of thinning during punching. While the approach reduces deviation between experimental observations and material property, however, it remains susceptible to errors, particularly under complex stress states. Later, an alternative approach was proposed which uses the full field deflection of the specimen mapped through in-situ digital image correlation [19]. Continuous monitoring of thinning, as demonstrated by Janca et al. [20] integrates advanced instrumentation to directly track deformation during testing. This allows for better understanding of thinning behaviour during SPT. Furthermore, Kuna and Abendroth [21] demonstrated the role of ductile damage models in capturing necking and thinning behaviour in SPT, incorporating finite element analysis. This will help with further research on thinning behaviour.

Even though thinning phenomenon may occur throughout the specimen, the effect is more obvious at the center of the specimen under low friction force. This location appears as a region with less constraints and thus higher deformation. This observation was verified by Cakan et al. [22] who developed a numerical model to investigate how the Grade P91 steel would deform during the small punch test. Later, Lee et al. [23] proposed a numerical model to simulate the thinning and fracture of a cracked pipe material using the small punch test. The model employs damage analysis based on the multi-axial fracture strain energy density. While some work has been performed to investigate the thinning phenomenon during the small punch test, insufficient data is available in literature to conclude the observation. Based on the author’s knowledge, the mechanism of how friction controls the thinning process is also not well discussed and understood.

This study aims to investigate the influence of plastic hardening and surface friction on the deformation and fracture behaviour of Grade 91 steel, considering the thinning process. The numerical modelling-based FE is developed, and the results are validated against experimental data from the literature. Various bi-linear stress-strain slopes are employed to represent the hardening value. Friction coefficients value is varied to manipulate the contact surface condition.

CONSTITUTIVE MATERIAL MODELS

Note that high temperature material such as 9Cr-1Mo, 9Cr-0.5Mo-1.8W-VNb steels typically exhibit Power’s law plastic hardening. In the present study, however, the material is assumed to deform into elastic and plastic manners following Hooke’s law and linear hardening (see Eqn. (9)) relations, respectively. The slope, H varies from zero (perfectly-plastic) to 6500 with intervals of 2000. The material constants of these relations are tabulated in Tab. 1.

$$\sigma(\varepsilon) = \begin{cases} E\varepsilon & \text{for } 0 \leq \varepsilon \leq \frac{S_y}{E} \\ S_y + H\left(\varepsilon - \frac{S_y}{E}\right) & \text{for } \frac{S_y}{E} \leq \varepsilon \leq \varepsilon_f \end{cases} \tag{2}$$

where, E is the Young’s modulus, ε is the strain, S_y is the yield strength, H is the slope of plastic hardening curve and ε_f is the fracture strain.

The friction between contacting surfaces (puncher-to-specimen and die-to-specimen) is modelled according to Coulomb friction theory [5]. This theory states that the shear stress is proportional to the contact pressure and can be mathematically expressed by Eqn. (3):

$$\tau = \mu P \tag{3}$$

where, τ is the shear stress, μ is the coefficient of friction, and P is the contact pressure. In the present study, the value of friction coefficient, μ varied from zero to 0.7. A zero-friction coefficient indicates that no shear forces is induced on the contact surface, therefore, these surfaces are free to slide. Meanwhile, a coefficient value of 0.7 implies frictional contact surface. The value of each parameter employed in the FE simulation is summarized in Tab. 1.

Parameter (unit)	Value
E (GPa)	213
ν	0.3
S_y (MPa)	512
H	0, 2500, 4500, 6500
ϵ_f (%)	8.5
μ	0, 0.2, 0.7

Table 1: Material constants employed in present study.

Fig. 1 shows the bi-linear stress-strain curve of the material employed in this study. The experimental stress-strain data [24] of Grade 91 steel, which obeys Power’s Law relation during plastic deformation, is also included in the figure for direct comparison. The yield strength, S_y and fracture strain are kept constant at 512 MPa and 8.5 %. The hardening slopes, H of 2500 and 4500 are chosen so that the curve lies between the experimental data. To account for variations in mechanical properties due to batch-to-batch and service conditions of the material, a perfectly plastic hardening ($H = 0$) and slightly higher hardening of $H = 6500$ are also simulated.

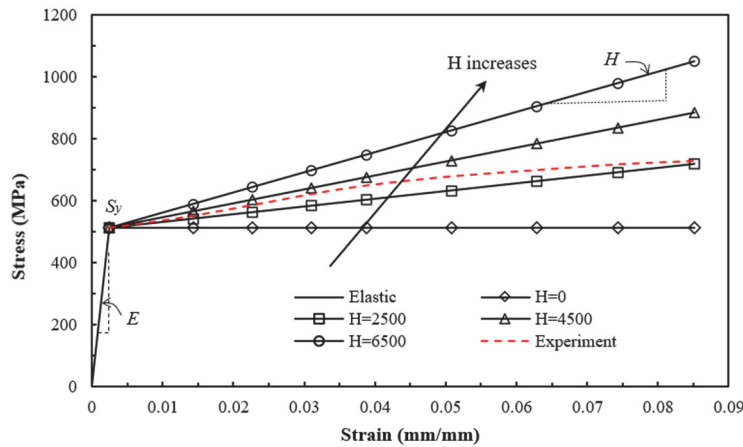


Figure 1: Effect of H parameter on the plastic hardening curve employed in the present study

FINITE ELEMENT MODELLING OF SMALL PUNCH TEST

Commercial finite element (FE) software of Abaqus v6.14 was employed to model the small punch test. The FE model comprises rigid upper and lower dies for specimen positioning and clamping, a rigid puncher (with a nose radius of 1.25 mm), and a deformable disc-shaped specimen. The specimen has a diameter and thickness of 8 mm and 0.5 mm, respectively. Considering the disc-shaped of the specimen, circular test rig and load symmetry, a 2-dimensional axis-symmetric model was constructed. While the axisymmetric model offers computational efficiency, it should be acknowledged that the model may not accurately capture the thinning behaviour particularly during the necking due to numerical regularization. The bi-linear constitutive material model with varying plastic slope, H (as shown in Fig. 1) was

employed. Furthermore, the friction coefficient, μ ranged from 0 (frictionless or smooth surface) to 0.7 (rough surface) was assigned to the interface between the puncher, upper/lower dies, and the specimen. Surface-to-surface contact was selected, and finite sliding model was chosen for sliding formulation. The axis-symmetric FE model of the small punch test setup including detailed dimensions, is illustrated in Fig. 2(a), while Fig. 2(b) presents the employed boundary conditions. The horizontal translation and α -rotational motion of the punch were constrained to zero, while a predefined displacement of 2.5 mm was imposed in the y -direction. Additionally, the lower die was constrained in all directions, and the upper die was constrained in the same manner as the puncher, except for predefined displacement. Instead, a clamping force of 500 N was applied to the upper die to simulate the tightening torque during experimental setup.

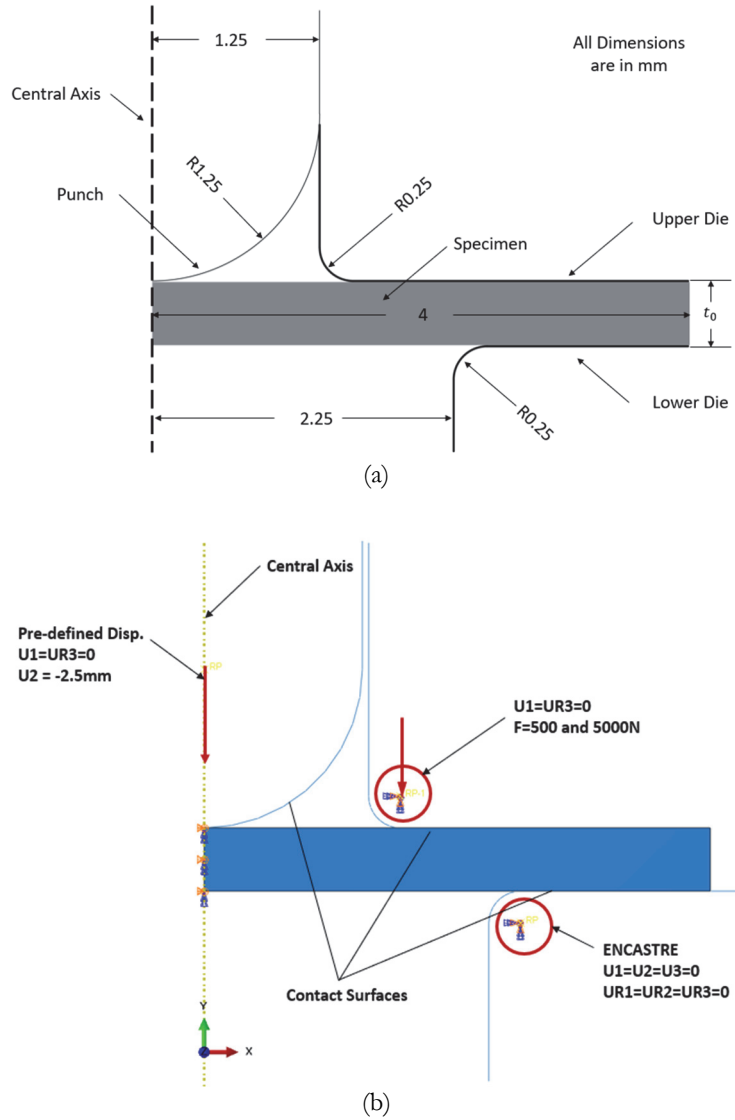


Figure 2: Small punch test setup: (a) detail dimension and (b) FE model.

The simulation was performed in two stages. In the first stage, a clamping force was applied to the disc specimen through the upper die. The obtained results for deformation and stress state were then exported to the second stage of the simulation using an initial predefined option in Abaqus software. In the second stage of simulation, the predefined displacement was applied to the disc specimen through the rigid semi-circular nose puncher. Continuum axis-symmetric 4-nodes with reduced integral elements (CAX4R) scheme were assigned to the specimen. A mesh sensitivity analysis was performed to determine the optimum mesh size. For the present study, the number of nodes and elements were 2617 and 1903, respectively. The simulation accounted for geometric nonlinearity and the automatic stabilization option was activated to minimize instabilities problems that could lead to non-convergence issue.

RESULT AND DISCUSSION

Fig. 3 shows the comparison of the force-displacement curve between experimental data [24] and FE prediction with various hardening levels. The displacement value is the vertical translation measured from the bottom centre of the specimen. Note that the FE results in Fig. 4 are obtained by incorporating friction coefficient of 0.2. This value has been reported to yield a good prediction for 9Cr steels [7]. However, for other materials, the friction coefficient value can be further calibrated. It can be observed that the curve exhibits several deformation stages including elastic and plastic bending deformation, membrane stretching, plastic instability, and fracture. Furthermore, the experimental data lies between the curve $H = 2500$ and $H = 4500$ (see Fig. 3). It is worth noting that better prediction can be achieved by calibrating the hardening slope, H .

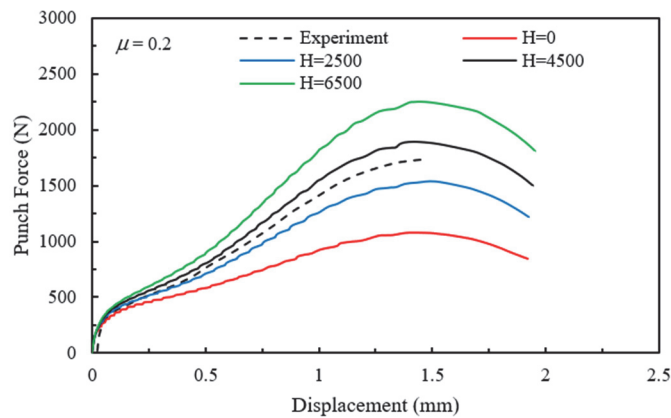


Figure 3: Comparison of load-displacement curve between experiment and FE.

Fig. 4 illustrates the deformation response under different hardening slopes and friction. Note that the curve is plotted up to 20 % force drop, which represents the failure point [1]. In general, the material exhibits a higher maximum load at higher hardening, H . This implies an increase in material resistance against deformation. This is due to the phenomenon that the dislocation density increases, and interactions between dislocations result in a higher stress required for further plastic deformation, leading to an increase in the material's strength and hardness. As shown in Fig. 4, both upper and lower node displacements are plotted to investigate the thinning of the material. The upper node (UN) and lower node (LN) at specimen's center which the displacement data is extracted are illustrated in Fig. 5. Thinning is then estimated using Eqn. (1). Thinning is observed to occur instantly as the load is applied and this process increases steadily up to fracture. Due to the thinning, less displacement at the lower node compared to the upper node is expected at a similar load level. Interestingly, the thinning of the material at maximum force, T_m remains unchanged under variation of H . However, there is evidence that thinning at fracture, T_f is affected by the hardening as shown in Fig. 4(b). Under the presence of friction, insignificant thinning at the specimen's center occurs as the surface friction increases. Considerable thinning is observed under smooth or frictionless surfaces. For frictionless surface contact, material slides freely under the application of punch load. In contrast, material deformation is restricted under rough surfaces at both contact surfaces i.e., puncher-specimen and die-specimen, consequently slowing down the thickness reduction rate at the center of the specimen. The thinning at this surface condition, is thus negligible (see Fig. 4(c)). However, friction leads to the development of necking at the contact surface between punch and specimen and affects the value of total displacement at fracture. Therefore, any attempt to evaluate the deformation of the material must consider this phenomenon. Further discussion on this phenomenon will be provided in the next section of the article.

A direct comparison of force-displacement curve between different values of the friction coefficient, ranging from 0 (frictionless) to 0.7 is shown in Fig. 7. At small punch displacement, the force-displacement curve remains almost identical for different μ values until a certain point of approximately 0.75 mm displacement. This is because, at this stage, the deformation of the specimen is predominantly controlled by bending and is less influenced by sliding, therefore the additional resistance due to friction on the contact surface is negligible. Since the material yield strength is usually estimated based on the maximum load during elastic bending, the value is unaffected by the friction. However, as the puncher moves further into the specimen, the curve starts to deviate from each other. A higher maximum force value is simulated as the friction coefficient increases. This implies the sliding took place and was influenced by the friction. For the case of $\mu = 0$, the specimen is free to deform without any constraint in the sliding direction. However, as the value of μ becomes non-



zero, additional resistance is observed due to friction between the contact surface of puncher-to-specimen and die-to-specimen.

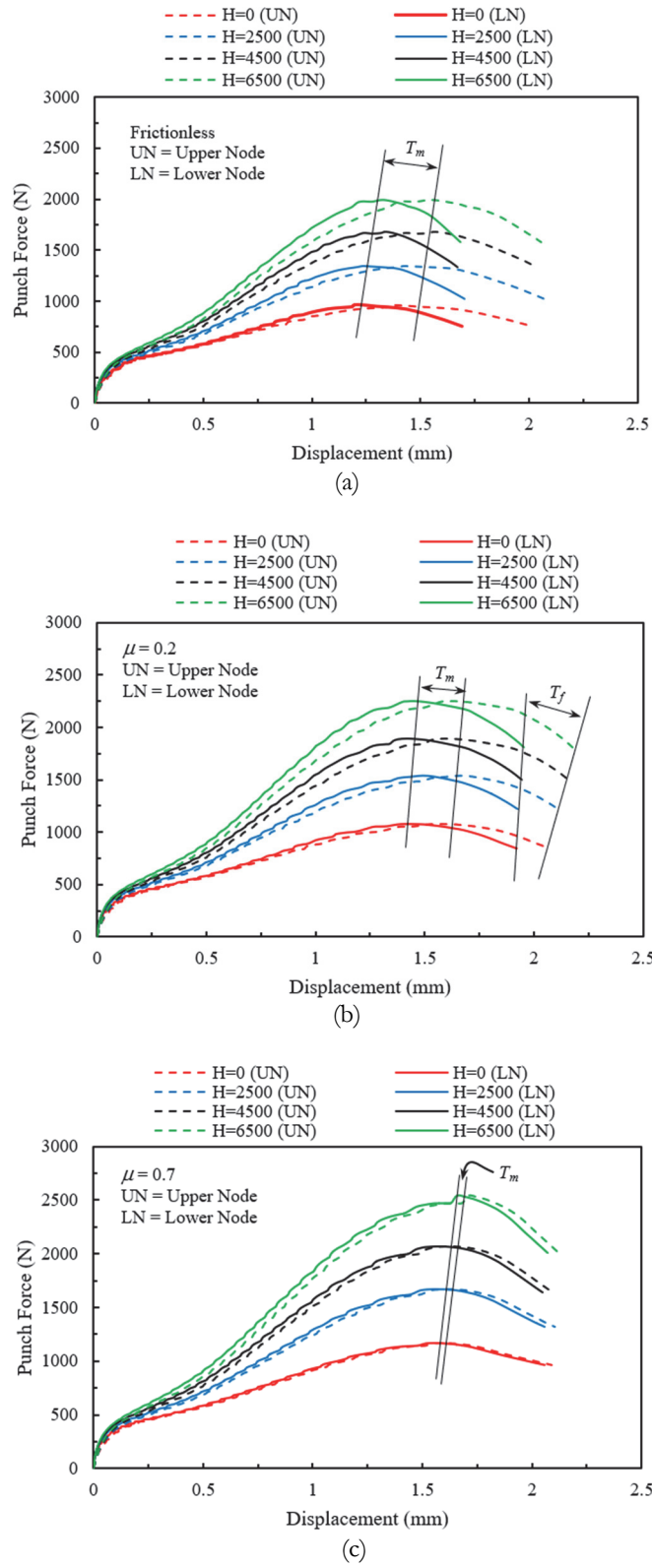


Figure 4: Effect of plastic hardening on force-displacement curve (a) $\mu = 0$ (frictionless), (b) $\mu = 0.2$ and (c) $\mu = 0.7$

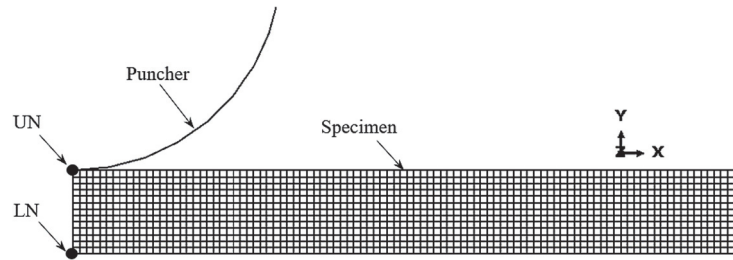


Figure 5: Upper and lower nodes in which the nodal displacement is extracted.

It is also observed in Fig. 6 that μ affects the maximum force. When $\mu = 0$, the simulated maximum force is 1.66 kN, while at $\mu = 0.2$ and 0.7 , the maximum force increases by approximately 14% and 25%, respectively. It is worth noting that the corresponding displacement at maximum force exhibits a similar increasing behaviour. The estimated displacement obtained from the simulation is 1.43 mm, 1.57 mm, and 1.64 mm at $\mu = 0$, $\mu = 0.2$ and $\mu = 0.7$, respectively. Furthermore, at higher values of μ , a slightly steeper force reduction is observed as the force reaches its maximum value. This is attributed to the faster evolution of necking in the material.

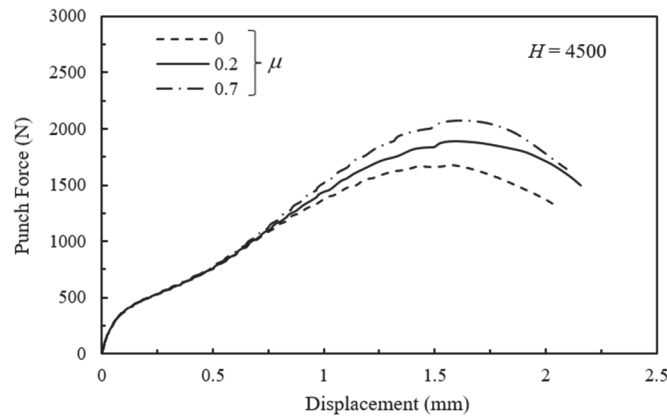


Figure 6: Effect of contact friction on displacement response at constant $H = 4500$.

As observed in the simulation results, the thickness of the specimen gradually decreases under the small punch load. This thinning phenomenon is further investigated to evaluate its role in fracture and deformation mechanisms. Fig. 7 shows the thinning evolution of the specimen under the influence of friction coefficient. The effect of plastic hardening on the thinning process is also included in Fig. 7. Note that upon load application, higher deformation occurs at the center while the value remains low at other regions depending on the stress distribution in the specimen. In fact, the upper surface of the specimen tends to deform more than the bottom surface. As a result, the reduction of thickness is observed as well as the thinning. Thinning can be determined as the displacement difference between the top and bottom surface (of the specimen) in the through thickness direction. In the present study, thinning is estimated at the center of the specimen. This point is usually used to measure the displacement of the material during experimental work. Additionally, the thinning is also estimated at the necking location to better understand its contribution towards fracture.

As seen in Fig. 7, the specimen with $\mu = 0$ suffers significant thinning at the center position. Up to the fracture point, the thickness of this specimen reduces by approximately 72%. At the early stage of elastic and plastic deformation, the rate of thinning is low regardless the value of μ . The thinning rate then increases rapidly during the membrane stretching stage for $\mu = 0$ and 0.2 (see Fig. 7 and Fig. 8). The thinning process continues at the same rate until fracture for the specimen with $\mu = 0$. In contrast, the thinning evolution of the material with $\mu = 0.7$ (see Fig. 9) remains at a lower rate starting from the beginning of deformation until fracture. Once the maximum force point is reached, no further thinning is observed for the specimen with $\mu = 0.2$ and 0.7 . This is due to the necking that developed at the position offset from the specimen center. The deformation mostly occurred at the necking area, and other locations remain undeformed. Therefore, no further thinning progress is observed at the center. The friction caused additional slipping constraints at the parallel plane of the contact surface. As a result, the specimen with higher μ yields the lowest thinning. It is found that the percentage of thinning for $\mu = 0.2$ and 0.7 are 42% and 10%, respectively.

The close-up of the small deformation region of the SP specimen is also drawn in Figs. 7 to 9. The figure indicates material thinning at the same rate until approximately 450 N punch load. At this stage, material deforms elastically. Depending on various intercept techniques [13] it has been reported that the yield load of P91 steel material lies at approximately 250 - 450N. Note that the yield strength of the specimen is usually estimated using the yield load value during elastic deformation stage. As the thinning during the elastic deformation remains constant regardless of the magnitude of friction and hardening, therefore, this observation is also valid for the yield strength. However, as the material deforms plastically, the data of thinning start to deviate from each other. This behaviour continues until the fracture point. The ultimate tensile strength value, which is usually derived based on the maximum load at the onset of tensile stability stage, may be affected by friction. Furthermore, it is also observed that the magnitude of plastic hardening mostly affects the thinning process during membrane stretching and plastic instability regions.

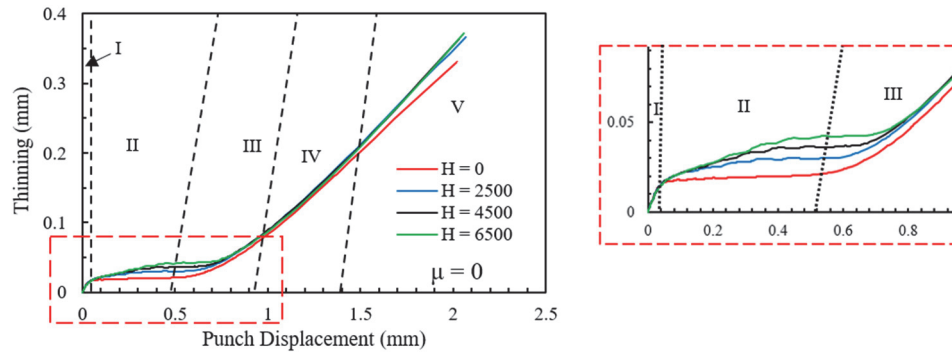


Figure 7: Effect of hardening on thinning at constant $\mu = 0$.

Fig. 8 illustrates the graph of thinning against punch displacement for $\mu = 0.2$ under the influence of plastic hardening. At the beginning of deformation, approximately between 0 mm and 0.04 mm, the material deforms in an elastic manner. No significant thinning is evident, similar to the case with a frictionless surface. As the deformation progresses further, between 0.04 mm and 0.5 mm, the plastic bending region initiates. Here, thinning continues to develop slowly but at a constant rate. Once punch reaches 0.5 mm to 1.1 mm displacement, the membrane stretching region begins. Thinning starts to increase more noticeably as the punch moves further. At this stage, thinning reaches its maximum value. As the punch goes beyond 1.1 mm, the plastic instability region initiates, and the thinning remains at its maximum value. As the deformation progresses, necking starts to initiate, and eventually the material breaks apart. Clearly, thinning increases with hardening, and its influence is obvious in the membrane stretching and plastic instability region.

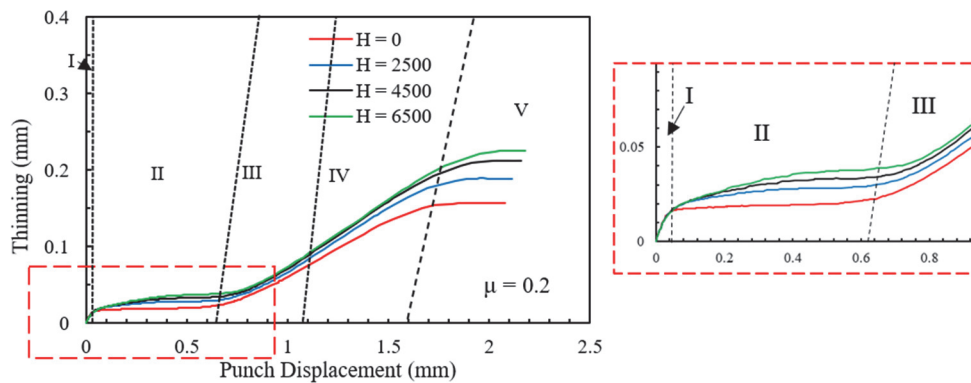


Figure 8: Effect of hardening on thinning at constant $\mu = 0.2$.

Fig. 9 shows the graph of thinning against punch displacement at a friction coefficient of 0.7 under varying hardening slope. In the elastic region (0 mm to 0.04 mm punch displacement), thinning is very minimal, at around 0.02 mm. In the plastic bending region (0.04–0.6 mm punch displacement), thinning slightly increases, however, the impact is somewhat negligible. A similar trend is evidenced during the membrane stretching region (0.6 to 1 mm punch displacement). Furthermore, it is also found that thinning behaviour follows the same trajectory from $H = 0$ to $H = 6500$. This trend can also be true in plastic instability and fracture zones. Observation from Fig. 7, Fig. 8, and Fig. 9 indicate that increase in hardening slope

leads to a higher thinning value, particularly during membrane stretching and plastic instability regions. Under the presence of friction, the thinning at the center of specimen reduced according to the friction level. In Fig. 10, thinning is plotted against punch force at a constant hardening slope of $H = 4500$ and varying friction coefficient. During the initial deformation stage, the thinning has a linear relationship with punch force. However, the increase in thinning is very minimal. For instance, when punch force increased up to 450 N the thinning increased just to 0.025 mm. The thinning rate then remains constant up to 1000 N. Further to this point, there is a significant rise in thinning until reaching the maximum load. The overall thinning behaviour is similar across all friction coefficients; however, specimens with lower friction or frictionless conditions exhibit a more significant reduction in thickness compared to those with higher friction. However, it is worth noting that using the current approach, the results obtained may over-/underestimate the thinning value during the final deformation stages of necking due to numerical regularization of axisymmetric model.

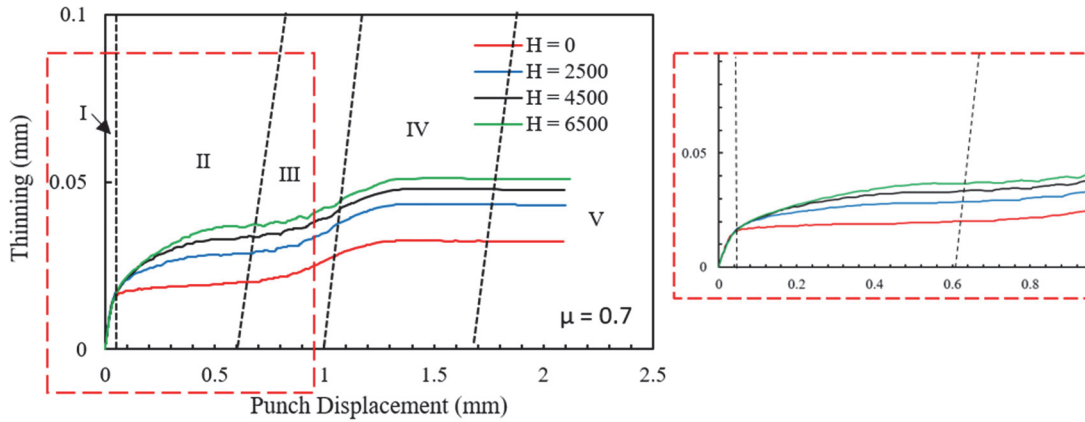


Figure 9: Effect of hardening on thinning at constant $\mu = 0.7$.

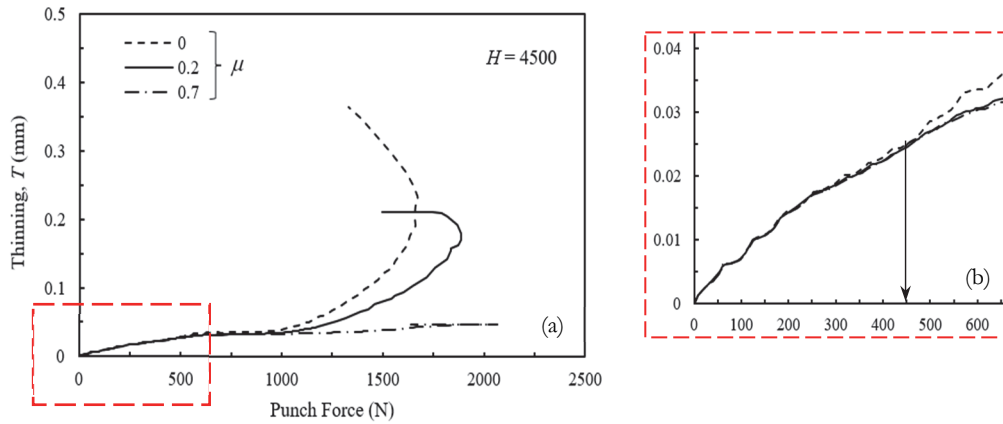


Figure 10: Evolution of thinning under the influence of friction at constant $H = 4500$: (a) full view and (b) close up at initial deformation stage.

Fig. 11 shows the evolution of deformation and thinning of specimen under small punch test. Here, the value of hardening parameter, H is 2500 and the friction coefficient between punch and specimen and die and specimen is zero. The image denotes the end of each deformation zone. Initially, the specimen deforms elastically, with both upper and lower surfaces showing small deformation, and thinning is not clearly observed. As the puncher further moves towards the specimen, local deformation occurs at the contact region between the sample and punch. Both upper and lower surfaces deform at almost similar rates. Under the membrane stretching deformation, the upper and lower surfaces at the contact region deform differently, possibly due to the variation of material constraint throughout the specimen's thickness. Thinning is observed particularly at the contact region. A similar observation is also found during the plastic instability region. In this zone, thinning significantly occurs and leads to final fracture of the specimen. With friction-free surface, the fracture is predicted to occur at the centre of the specimen. Fig. 12 shows an illustration of the direction of stress that controls the deformation and thinning.

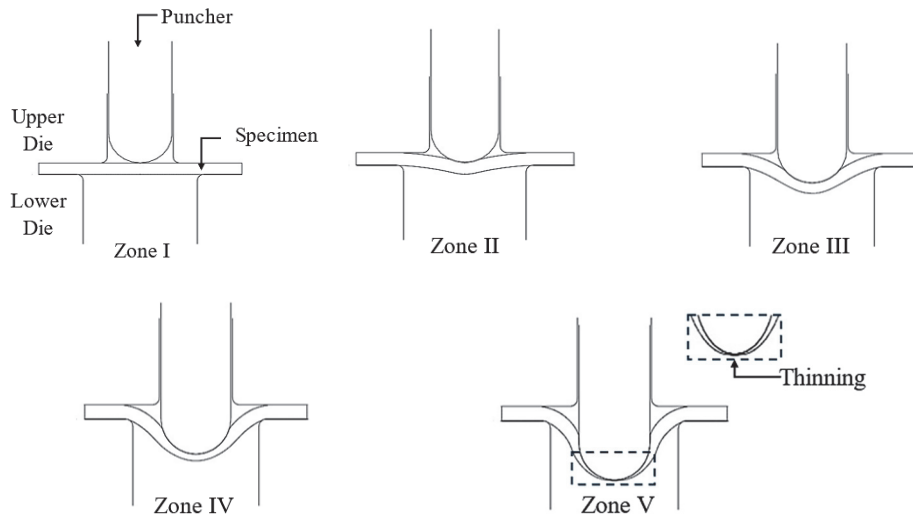


Figure 11: Evolution of deformation when friction coefficient, $\mu = 0$.

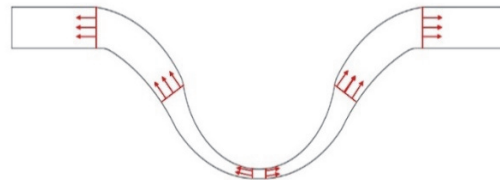


Figure 12: An illustration of the direction of the stress-controlled deformation with $\mu = 0$.

Fig. 13 displays the evolution of deformation at different zones under the influence of surface contact friction. The hardening slope of the material and friction coefficient are 2500 and 0.2, respectively. The deformation shape of the specimen at the end of each distinct deformation zone is presented. In the first two deformation zones, the specimen's deformation remains similar to the case with no friction, with insignificant thinning observed. However, as the deformation enters zone III of membrane stretching, the thinning rate at the specimen's centre slows down compared to the frictionless specimen, while necking develops at a location offset from the centre. The necking becomes significantly exposed in zone IV as the puncher moves towards the bottom of lower die. At the centre of the specimen, thinning is still observed, but its rate decreases and finally stops before entering zone V of deformation. Due to necking, the load-bearing capacity of the material drops, leading to fracture. It is worth highlighting that the contribution of thinning to fracture control diminishes as the necking starts to induce in the material.

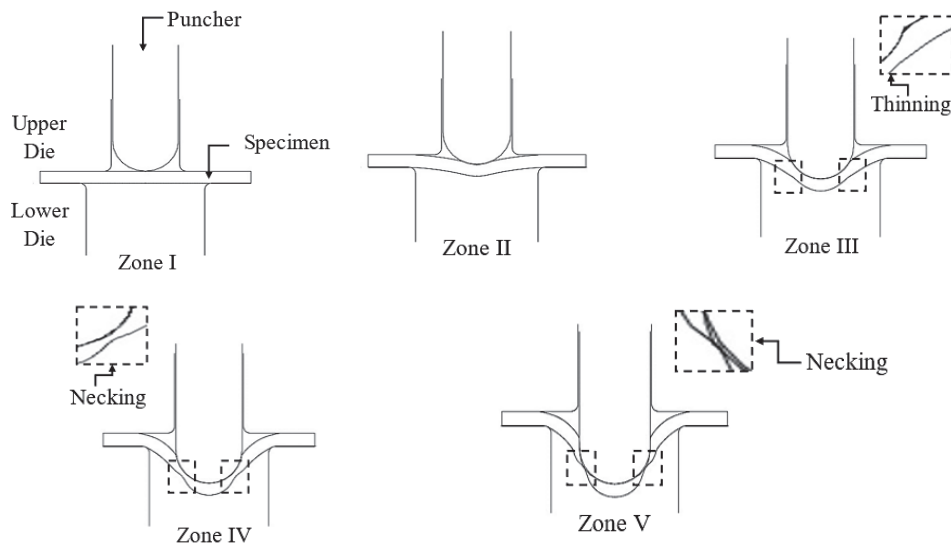


Figure 13: Evolution of deformation when friction coefficient, $\mu = 0.2$.

Fig. 14 illustrates the deformation and necking processes observed for hardening slope $H = 2500$ and a friction coefficient of 0.7. Each image in Fig. 14 indicates the evolution of the specimen's shape at distinct stage of deformation. Increasing the μ from 0.2 to 0.7 does not notably change the overall deformation and thinning behaviour of the specimen, except for the early development of necking. Due to this reason, the progression of thinning slows down even at an early stage of deformation. Thinning at the centre of the specimen remains unchanged until the fracture point. Under $\mu = 0.7$, thinning is still dominant in the membrane stretching zone, similar to other levels of friction. Fig. 15 displays the direction of stress-controlled deformation, leading to thinning and material instability of necking.

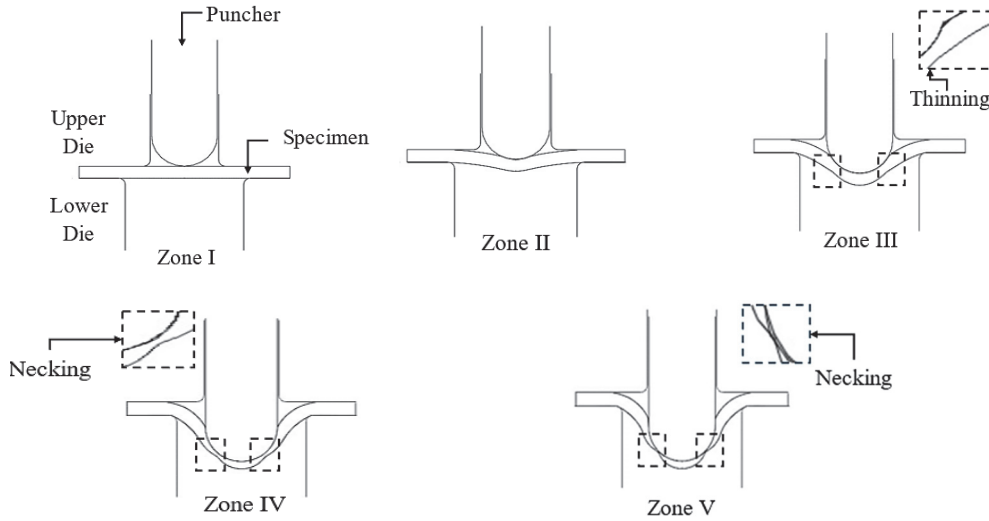


Figure 14: Evolution of deformation when friction coefficient, $\mu = 0.7$.

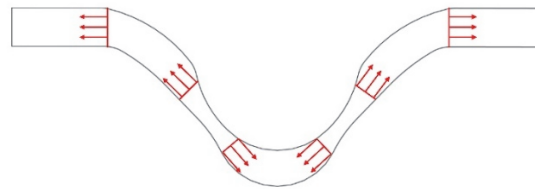


Figure 15: An illustration of the direction of stress-controlled deformation with $\mu = 0.7$.

To summarize, at $\mu = 0$, necking does not occur, and thinning progresses from the initial deformation until fracture zone. Thinning is more obvious at the contact zone between puncher and the specimen. However, under the presence of friction force, necking overrules thinning and is responsible for further deformation behaviour of the material in small punch tests. This observation suggests that as the load applies to the specimen, the frictional force obstructs the punch deformation of the contact zone. This high frictional force is favoring sticking the punch to the material rather than deforming it, which hinders further deformation and promotes additional constraints at the contact areas. As a result, necking is observed at the contact region, where the stress difference is high. Chen et al. [25] describe this phenomenon in microstructural scale behaviour. They found that the voids and recovered grains align in a certain direction and elongate after achieving maximum load.

Fig. 16 (a) and (b) depict the effect of hardening on thinning at the necking region, with the friction coefficient set at $\mu=0.2$ and 0.7, respectively. The results clearly show that the thinning behaviour at the fracture point differs from the behaviour found at the center of the specimen (see Figs. 7 to 9). Thinning occurs at all deformation stages regardless of the hardening slope value. Under perfectly plastic and low hardening conditions, thinning is higher compared to cases with higher hardening. Interestingly, this phenomenon is not consistent as deformation progresses. Higher hardening values yield higher thinning at displacement of 1.25 mm and 0.6 mm for $\mu=0.2$ and 0.7, respectively. Comparing Fig. 16 (a) and (b), the presence of higher friction drives greater thinning at the necking regions. This observation can be explained based on the necking behaviour. As the load continues, the region with the smallest cross-sectional area (the neck) experiences higher stress than

the surrounding areas. The higher stress concentration at the necking leads to increased thinning, especially under higher friction conditions.

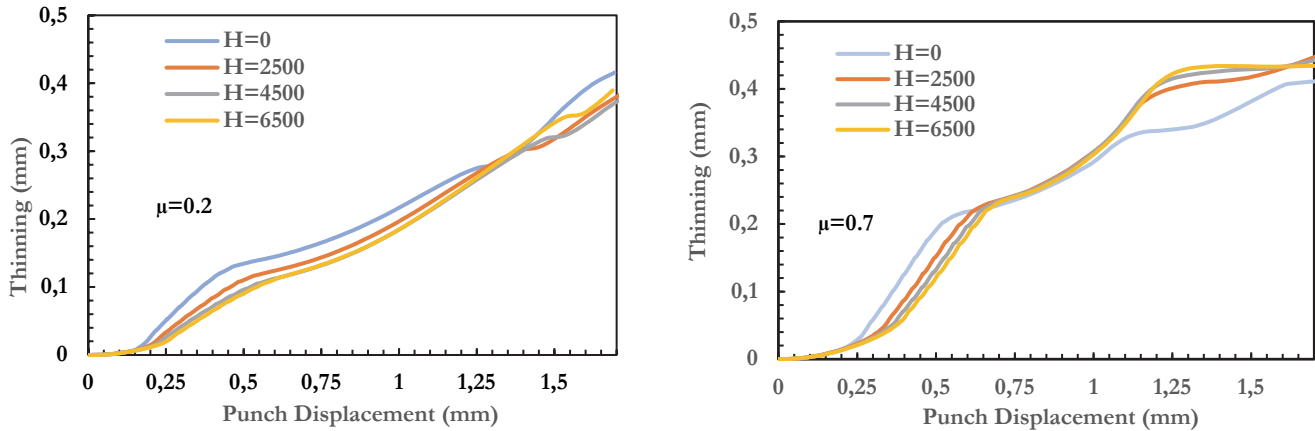


Figure 16: Effect of hardening on thickness reduction at necking region: (a) at $\mu = 0.2$ and (b) $\mu = 0.7$

Fig. 17 shows the stress distribution on the specimen obtained from FE simulation with different hardening parameters and friction coefficient values. The contours are plotted at fracture point, approximately 20 % of the load drop [1]. It is observed that the von-Mises stress distribution is almost the same for both $H = 2500$ and $H = 4500$. However, the magnitude of stress is higher for $H = 4500$. At the center of the specimen with $\mu = 0$, the stress reached 730 MPa and 885 MPa for $H = 2500$ and $H = 4500$, respectively. The lowest stress occurs at the clamping area, at approximately 500 MPa, where the material remains elastic.

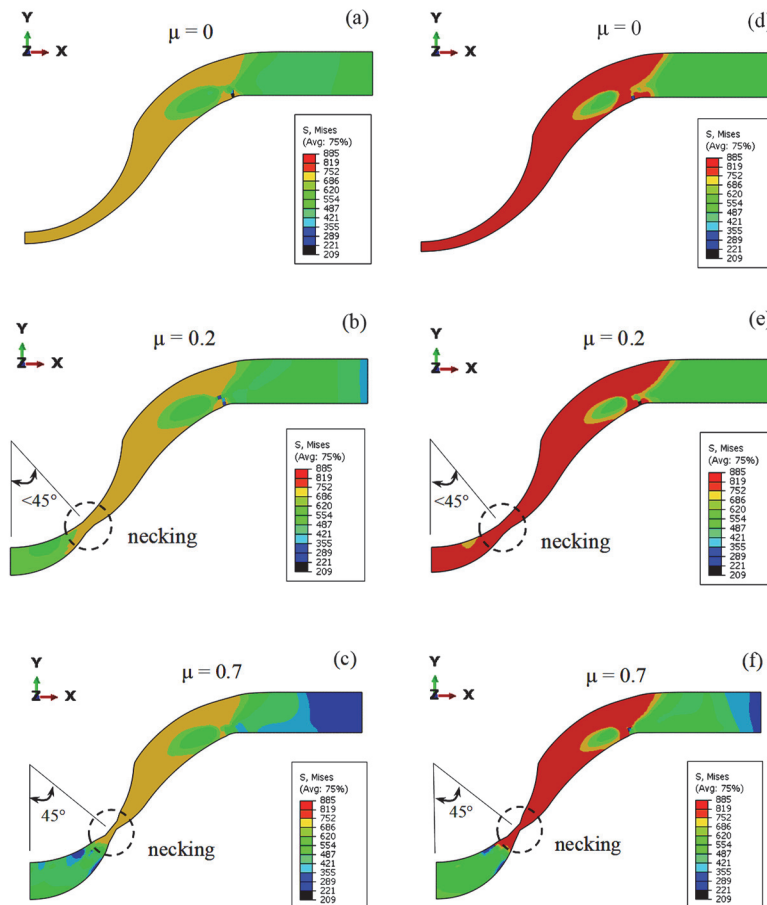


Figure 17: von-Mises stress contour: (a - c) $H = 2500$ and (d - f) $H = 4500$



For the case $\mu = 0$, the stress distribution at the punch area is more uniform. As the friction coefficient on the contact surface increases, stress becomes more complex due to the contribution of shear stress along the meridional direction of the specimen. Thinning is observed under frictionless conditions at the center of the specimen. As the punch penetrates, it stretches and thins the material, consistently reducing the thickness of the specimen, particularly at the center position of the indentation. This process continues, causing the cross-sectional area to drop along with the load-bearing capacity of material. This behaviour persists up to the fracture point. The fracture occurs at the center of the specimen, which is inconsistent with the one found in the experiment [25]. This suggests that friction between the puncher/specimen and die/specimen existed and significantly influenced the fracture behaviour. In contrast, the specimen with contact friction exhibits different behaviour. Friction caused additional resistance to deformation in the meridional direction from both contact regions of puncher and dies. Consequently, necking is observed, and the effect becomes more pronounced as the friction increases. It is also observed that when friction coefficient is 0.7, the fracture occurs at approximately 45° , measured from the vertical (y -axis) of specimen center. This location corresponds to the middle location between puncher edge or the boundary between contact-to-non-contact region and specimen's center. However, when the coefficient reduces to 0.2, this angle is simulated to occur at slightly less than 45° . This implies the contribution of prior thinning before the initiation of the necking.

CONCLUSION

The influence of plastic hardening and surface contact friction on the deformation response of materials under small-punch load has been studied. The role of thinning in determining the overall deformation and fracture behaviour is also discussed. It is found that plastic hardening insignificantly controls the thinning process but adds internal resistance to the deformation. Consequently, a higher maximum load is observed in the force-displacement curve of the small-punch test. In contrast, surface contact friction controls the thinning process and deformation of the material, particularly at low friction values. Furthermore, it is observed that thinning is dominant during the membrane stretching and plastic instability stage of deformation. Due to additional force induced by friction, necking initiates at the contact surface between the punch and the specimen, offset from the center point. This necking slows down the progression of thinning at the center of the specimen, resulting in a lower thinning value. Furthermore, the thinning evolution is found to behave differently depending on the specific location of the specimen. This discrepancy is due to the complex stress distribution and the influence of the necking on the adjacent area. Clearly, the common practice of deformation measurement at the center bottom surface of the specimen leads to errors when thinning is present.

The use of axisymmetric modeling in this study, while computationally efficient, introduces inherent limitations in representing non-axisymmetric behaviors. As mentioned earlier, these limitations may influence the accuracy of the results, particularly during the last stages of deformation. Despite this, the findings provide novel insight into the mechanics of small punch test by addressing the interdependence of plastic hardening, surface friction, and thinning behaviour. To further validate the current simplified axisymmetric model, future work should incorporate a 3-dimensional (3D) modeling approach that could minimize the limitation of axis-symmetric space due to numerical regularization and provide realistic modeling particularly during necking.

ACKNOWLEDGEMENT

The authors would like to express gratitude to the Universiti Malaysia Pahang Al-Sultan Abdullah (UMPSA) for funding this research under the Internal Grant RDU220361 and Ministry of Higher Education (MOHE) Malaysia for additional funding under Fundamental Research Grant Scheme FRGS/1/2023/TK10/UMP/02/11 (University reference RDU230109).

REFERENCES

- [1] Arunkumar, S. (2020). Overview of Small Punch Test, *Met. Mater. Int.*, 26(6), pp. 719–738, DOI: 10.1007/S12540-019-00454-5.
- [2] Ferdous, I.U., Alang, N.A., Alias, J., Nadzir, S.M. (2021). Numerical Prediction of Creep Rupture Life of Ex-Service and As-Received Grade 91 Steel at 873 K, *Int. J. Automot. Mech. Eng.*, 18(3), pp. 8845–8858,



- DOI: 10.15282/ijame.18.3.2021.01.0678.
- [3] Cheng, Z., Sun, J., Tai, P., Zhang, L., Wei, Y., Chang, H., Thuku, R., Gichuhi, K.M. (2021). Comparative Study between Small Punch Tests and Finite Element Analysis of Miniature Steel Specimens, *J. Mater. Eng. Perform.*, 30(12), pp. 9094–9107, DOI: 10.1007/S11665-021-06098-0.
- [4] Alang, N.A., Ferdous, I.U., Alias, J., Razak, N.A.A., Ahmad, A.H. (2024). On the Influence of Clamping Force and Contact Friction in Small Punch Test, *Lect. Notes Mech. Eng.*, pp. 175–182, DOI: 10.1007/978-981-97-4806-8_15.
- [5] Campitelli, E.N., Spätig, P., Bonadé, R., Hoffelner, W., Victoria, M. (2004). Assessment of the constitutive properties from small ball punch test: experiment and modeling, *J. Nucl. Mater.*, 335(3), pp. 366–378, DOI: 10.1016/j.jnucmat.2004.07.052.
- [6] Yang, S., Zhou, J., Ling, X., Yang, Z. (2012). Effect of geometric factors and processing parameters on plastic damage of SUS304 stainless steel by small punch test, *Mater. Des.*, 41, pp. 447–452, DOI: 10.1016/J.MATDES.2012.05.029.
- [7] Cortellino, F., Sun, W., Hyde, T. (2016). On the effects of friction modelling on small punch creep test responses: A numerical investigation, *J. Strain Anal. Eng. Des.*, 51(7), pp. 493–506, DOI: 10.1177/0309324716655661.
- [8] Prakash, R. V., Arunkumar, S. (2016). Influence of Friction on the Response of Small Punch Test, *Trans. Indian Inst. Met.*, 69(2), pp. 617–622, DOI: 10.1007/S12666-015-0769-4/FIGURES/8.
- [9] Samaee, V., Gatti, R., Devincre, B., Pardoën, T., Schryvers, D., Idrissi, H. (2018). Dislocation driven nanosample plasticity: new insights from quantitative in-situ TEM tensile testing, *Sci. Rep.*, 8(1), pp. 12012, DOI: 10.1038/s41598-018-30639-8.
- [10] Yang, M.X., Yuan, F.P., Xie, Q.G., Wang, Y.D., Ma, E., Wu, X.L. (2016). Strain hardening in Fe–16Mn–10Al–0.86C–5Ni high specific strength steel, *Acta Mater.*, 109, pp. 213–222, DOI: 10.1016/j.actamat.2016.02.044.
- [11] Choudhary, B.K., Palaparti, D.P.R., Samuel, E.I. (2013). Analysis of Tensile Stress-Strain and Work-Hardening Behavior in 9Cr-1Mo Ferritic Steel, *Metall. Mater. Trans. A*, 44(1), pp. 212–223, DOI: 10.1007/s11661-012-1385-0.
- [12] Tantideeravit, S., Kamaya, M. (2020). An application of FEM in the determination of tensile properties for work-hardened carbon steel by means of small punch test, *Results Mater.*, 8, pp. 100142, DOI: 10.1016/j.rinma.2020.100142.
- [13] Calaf-Chica, J., Sánchez Palomar, M., Bravo Díez, P.M., Preciado Calzada, M. (2021). Deviations in yield and ultimate tensile strength estimation with the Small Punch Test: Numerical analysis of pre-straining and Bauschinger effect influence, *Mech. Mater.*, 153, DOI: 10.1016/j.mechmat.2020.103696.
- [14] Sánchez-Ávila, D., Barea, R., Martínez, E., Blasco, J.R., Portolés, L., Carreño, F. (2018). Determination of the instantaneous strain rate during small punch testing of 316 L stainless steel, *Int. J. Mech. Sci.*, 149, pp. 93–100, DOI: 10.1016/j.ijmecsci.2018.09.042.
- [15] Peng, Y., Cai, L., Chen, H., Bao, C. (2018). A new method based on energy principle to predict uniaxial stress–strain relations of ductile materials by small punch testing, *Int. J. Mech. Sci.*, 138–139, pp. 244–249, DOI: 10.1016/j.ijmecsci.2018.02.011.
- [16] Rasche, S., Kuna, M. (2015). Improved small punch testing and parameter identification of ductile to brittle materials, *Int. J. Press. Vessel. Pip.*, 125, pp. 23–34, DOI: 10.1016/j.ijvp.2014.09.001.
- [17] Buljak, V., Cocchetti, G., Cornaggia, A., Maier, G. (2018). Parameter identification in elastoplastic material models by Small Punch Tests and inverse analysis with model reduction, *Meccanica*, 53(15), pp. 3815–3829, DOI: 10.1007/s11012-018-0914-3.
- [18] Egan, P., Whelan, M.P., Lakestani, F., Connelly, M.J. (2007). Small punch test: An approach to solve the inverse problem by deformation shape and finite element optimization, *Comput. Mater. Sci.*, 40(1), pp. 33–39, DOI: 10.1016/j.commsci.2006.10.021.
- [19] Vijayanand, V.D., Mokhtarishirazabad, M., Peng, J., Wang, Y., Gorley, M., Knowles, D.M., Mostafavi, M. (2020). A novel methodology for estimating tensile properties in a small punch test employing in-situ DIC based deflection mapping, *J. Nucl. Mater.*, 538, pp. 152260, DOI: 10.1016/j.jnucmat.2020.152260.
- [20] Janča, A., Siegl, J., Haušild, P. (2016). Small punch test evaluation methods for material characterisation, *J. Nucl. Mater.*, 481, pp. 201–213, DOI: 10.1016/j.jnucmat.2016.09.015.
- [21] Abendroth, M., Kuna, M. (2006). Identification of ductile damage and fracture parameters from the small punch test using neural networks, *Eng. Fract. Mech.*, 73(6), pp. 710–725, DOI: 10.1016/j.engfracmech.2005.10.007.
- [22] Çakan, B.G., Soyarslan, C., Bargmann, S., Hähner, P. (2017). Experimental and Computational Study of Ductile Fracture in Small Punch Tests, *Mater.*, 10(10), pp. 1185, DOI: 10.3390/MA10101185.
- [23] Lee, J.M., Hwang, J.H., Kim, Y.J., Kim, J.W. (2021). Predicting ductile fracture of cracked pipes using small punch test data, *Eur. J. Mech. - A/Solids*, 87, pp. 104211, DOI: 10.1016/J.EUROMECHSOL.2021.104211.
- [24] Ruiz-Moreno, A., Hähner, P., Fumagalli, F., Haiblikova, V., Conte, M., Randall, N. (2020). Stress–strain curves and derived mechanical parameters of P91 steel from spherical nanoindentation at a range of temperatures, *Mater. Des.*,



194, pp. 108950, DOI: 10.1016/J.MATDES.2020.108950.

- [25] Chen, H., Yang, R., Al-Abedy, H.K., Li, H., Sun, W., Jones, I.A. (2020). Characterisation of deformation process and fracture mechanisms of P91 steel at 600 °C in small punch tensile testing, *Mater. Charact.*, 168, DOI: 10.1016/j.matchar.2020.110514.